



**HAL**  
open science

## End of range defects in Ge

S. Koffel, Nikolay Cherkashin, Florent Houdellier, Martin Hÿtch, Gérard Benassayag, P. Scheiblin, Alain Claverie

► **To cite this version:**

S. Koffel, Nikolay Cherkashin, Florent Houdellier, Martin Hÿtch, Gérard Benassayag, et al.. End of range defects in Ge. *Journal of Applied Physics*, 2009, 105, pp.126110. 10.1063/1.3153985 . hal-01736054

**HAL Id: hal-01736054**

**<https://hal.science/hal-01736054>**

Submitted on 23 Mar 2018

**HAL** is a multi-disciplinary open access archive for the deposit and dissemination of scientific research documents, whether they are published or not. The documents may come from teaching and research institutions in France or abroad, or from public or private research centers.

L'archive ouverte pluridisciplinaire **HAL**, est destinée au dépôt et à la diffusion de documents scientifiques de niveau recherche, publiés ou non, émanant des établissements d'enseignement et de recherche français ou étrangers, des laboratoires publics ou privés.

## End of range defects in Ge

S. Koffel, N. Cherkashin, F. Houdellier, M. J. Hytch, G. Benassayag, P. Scheiblin, and A. Claverie

Citation: *Journal of Applied Physics* **105**, 126110 (2009); doi: 10.1063/1.3153985

View online: <https://doi.org/10.1063/1.3153985>

View Table of Contents: <http://aip.scitation.org/toc/jap/105/12>

Published by the [American Institute of Physics](#)

---

### Articles you may be interested in

[Diffusion of n-type dopants in germanium](#)

*Applied Physics Reviews* **1**, 011301 (2014); 10.1063/1.4838215

[Diffusion, activation, and recrystallization of boron implanted in preamorphized and crystalline germanium](#)

*Applied Physics Letters* **87**, 172109 (2005); 10.1063/1.2117631

[End-of-range defects in germanium and their role in boron deactivation](#)

*Applied Physics Letters* **97**, 012105 (2010); 10.1063/1.3456537

[Amorphization kinetics of germanium during ion implantation](#)

*Journal of Applied Physics* **105**, 013528 (2009); 10.1063/1.3041653

[Mechanisms of boron diffusion in silicon and germanium](#)

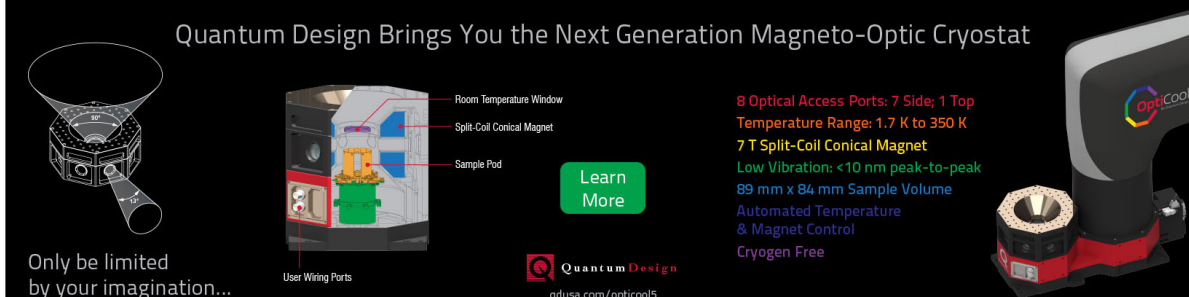
*Journal of Applied Physics* **113**, 031101 (2013); 10.1063/1.4763353

[Activation and diffusion studies of ion-implanted \*p\* and \*n\* dopants in germanium](#)

*Applied Physics Letters* **83**, 3275 (2003); 10.1063/1.1618382

---

Quantum Design Brings You the Next Generation Magneto-Optic Cryostat



Only be limited by your imagination...

Learn More

Quantum Design  
qdusa.com/opticool5

8 Optical Access Ports: 7 Side; 1 Top  
Temperature Range: 1.7 K to 350 K  
7 T Split-Coil Conical Magnet  
Low Vibration: <10 nm peak-to-peak  
89 mm x 84 mm Sample Volume  
Automated Temperature & Magnet Control  
Cryogen Free

## End of range defects in Ge

S. Koffel,<sup>1,2</sup> N. Cherkashin,<sup>1</sup> F. Houdellier,<sup>1</sup> M. J. Hytch,<sup>1</sup> G. Benassayag,<sup>1</sup> P. Scheiblin,<sup>2</sup> and A. Claverie<sup>1,a)</sup>

<sup>1</sup>*Mat Group, CEMES/CNRS, University of Toulouse, 29 Rue J. Marvig, 31055 Toulouse Cedex, France*

<sup>2</sup>*CEA-LETI, Minatec, 17 Rue des Martyrs, 38054 Grenoble Cedex 9, France*

(Received 4 February 2009; accepted 20 May 2009; published online 25 June 2009)

We show that the solid-phase epitaxial regrowth of amorphous layers created by ion implantation in Ge results in the formation of extended defects of interstitial-type. During annealing, these defects evolve in size and density following, as in Si, an Ostwald ripening mechanism. However, this process becomes nonconservative as the annealing temperature increases to 600 °C. This suggests that the recombination/annihilation of Ge interstitial atoms becomes important at these temperatures. These results have important implications for the modeling of diffusion of implanted dopants in Ge. © 2009 American Institute of Physics. [DOI: [10.1063/1.3153985](https://doi.org/10.1063/1.3153985)]

As the performance of metal-oxide-semiconductor transistors continue to evolve, the use of high-mobility channel materials such as Ge are being reconsidered as the semiconductor of choice. Unfortunately, little is known in comparison to Si of the basic mechanisms involved in the processing of Ge. The controlled doping of germanium by ion implantation is one of these processes which requires basic research before optimization. As in Si, high-dose ion implantation in Ge may result in the amorphization of the crystalline lattice.<sup>1,2</sup> These amorphous layers can be recrystallized by solid-phase epitaxy regrowth (SPER) during annealing, promoting the incorporation of dopant atoms into substitutional sites.<sup>1,3</sup>

In Si, it is well-documented that during such annealing, end of range (EOR) defects form below the initial crystalline/amorphous (c/a) interface.<sup>4</sup> These defects have been extensively studied in the past because they are responsible for current leakage in electrical junctions. Moreover, their thermal evolution during annealing is at the origin of transient anomalies of dopant diffusion [Ref. 4 and references therein]. EOR defects in Si are extrinsic i.e., interstitial defects which result from the precipitation of the large supersaturations of Si interstitial atoms remaining below the c/a interface just after ion implantation.<sup>5</sup> During annealing, these defects evolve in size and density following an Ostwald ripening mechanism involving the interchange of the contained Si atoms. Growth begins from clusters of 4 and 8 Si atoms<sup>6</sup> to the well-known rodlike {113} defects<sup>7</sup> and eventually dislocation loops of different types.<sup>8,9</sup> At the same time, the region containing the defects behaves as a time-decaying source of self-interstitials which enhances the diffusivity of some dopants by orders of magnitude.<sup>10</sup> This description has been introduced in modern process simulators to simulate diffusion of dopants in silicon after ion implantation and during annealing.<sup>11,12</sup>

Surprisingly, EOR defects have not yet been observed in Ge after the full SPER of continuous amorphous layers. Such layers have been imaged by different groups using cross-sectional transmission electron microscopy (XTEM) under

bright field or high resolution conditions but did not reveal any defects in the layers.<sup>1,13–15</sup> One paper<sup>16</sup> reported on the formation of extended defects after annealing of an amorphous layer in Ge but this layer was buried between two crystalline layers so that most of the observed defects resulted from the imperfect matching of the two c/a interfaces following regrowth. There are even suggestions that EOR defects might not form at all in Ge owing to the large vacancy concentrations which exist under equilibrium conditions in Ge at usual process temperatures.<sup>17,18</sup> For this reason, only vacancy-mediated diffusion is generally considered in Ge. Whether or not extrinsic EOR defects may exist in Ge is thus of major importance as it will determine whether the observed large diffusivities of implanted dopants<sup>19–23</sup> can only be ascribed to vacancies or might also be ascribed to an interstitial component of the diffusivity which, under equilibrium conditions, cannot be observed. Such considerations will guide the theoretical approach to simulate dopant diffusion in Ge after ion implantation. In this short paper, we demonstrate that EOR defects do form in Ge and are very small and much less stable than in Si. We provide an indirect but convincing proof that they are of interstitial-type.

(100) Ge wafers with resistivities in the 0.1–10 Ω cm range were implanted with Ge<sup>+</sup> at 150 keV and 5 × 10<sup>14</sup> ions/cm<sup>2</sup> or with P at 15 keV and 1 × 10<sup>15</sup> ions/cm<sup>2</sup> at a temperature of 270 K. These wafers were cut into pieces and annealed for a large variety of conditions (isochronal and isothermal annealing) in a “hot plate” furnace under N<sub>2</sub> atmosphere. The temperature ramping up and ramping down rates were of 5 °C/min. The annealing times reported in this study correspond to the “holding times” at the given temperatures and do not include the ramping times. The annealing temperatures were calibrated through the measurement by TEM of the velocity of the SPER of the amorphous layers<sup>3</sup> created by self-implantation. Finally, TEM specimens for plan-view (PV) and cross-sectional (X) observations were prepared by a combination of mechanical grinding and ion milling. As the final structure of the specimens is often affected by local heating, ion milling was performed at liquid N<sub>2</sub> temperature and/or using low ion fluxes. Samples were imaged using a Jeol 2010 microscope under weak beam dark field (WBDF) conditions with

<sup>a)</sup>Electronic mail: [alain.claverie@cemes.fr](mailto:alain.claverie@cemes.fr).

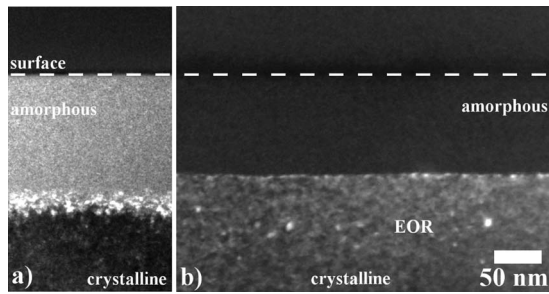


FIG. 1. WBDF-XTEM images of a Ge layer (a) after  $150 \text{ keV Ge}^+ 5 \times 10^{14} \text{ ions/cm}^2$  implantation and (b) after subsequent annealing at  $330 \text{ }^\circ\text{C}$  for 1325 s. The broken line follows the surface of the wafer. All images were taken under  $g, 2g$  using  $g=400$ .

$g=400$ . Some samples were imaged using the new electron holography technique capable of measuring strain in crystals with nanometer resolution and high accuracy.<sup>24</sup> Experiments were carried out on the SACTEM-Toulouse, a Tecnai F20 (FEI) equipped with aberration corrector (CEOS), field emission gun and electrostatic biprism. Holograms were analyzed using in-house software and GPA Phase 2.0 (HREM Research), a plug-in for the DigitalMicrograph image processing package (GATAN).

Figure 1(a) shows a XTEM image of the amorphous layer after Ge implantation. The  $c/a$  interface appears rough and heavily strained as evidenced by the white contrast in the WBDF image. After annealing at  $330 \text{ }^\circ\text{C}$  for 1325 s, the  $c/a$  interface has shifted by about 35 nm due to the SPER of the amorphous layer [Fig. 1(b)]. Small white dots are clearly visible under specific WBDF conditions ( $g, 2g, g=400$ ) in the region located just below the original  $c/a$  interface. Such contrast arises from the distorted area of the crystalline network surrounding small defects and is similar to the contrast observed around EOR defects in silicon.<sup>4</sup> The same defects were found in the  $P^+$ -implanted samples after similar annealing (not shown). However, the defects were located much closer to the surface, as the amorphous layer created by low energy  $P^+$ -implantation is much thinner (40 nm thick). The position of these defects is thus more favorable for observation in PV samples under WBDF conditions. For this reason, only results from  $P^+$ -implanted samples are shown subsequently.

Figure 2 is a set of PV micrographs showing the effect of increasing the annealing time at a fixed temperature on the population of defects found after  $P^+$ -implantation. As the annealing time increases from 10 to 60 s, the defects increase in

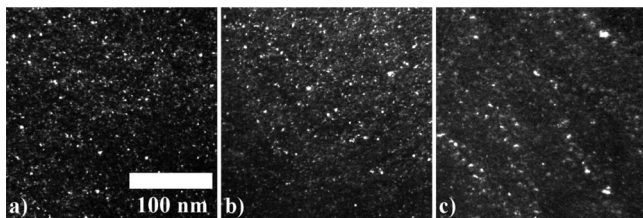


FIG. 2. Set of WBDF-PVTEM images showing the effect of annealing time on the population of EOR defects formed by  $15 \text{ keV } P^+$  and  $1 \times 10^{15} \text{ ions/cm}^2$  implantation. Samples annealed at  $380 \text{ }^\circ\text{C}$  for 30 s then at  $500 \text{ }^\circ\text{C}$  for (a) 10, (b) 30, and (c) 60 s. All images were taken under  $g, 3g$  using  $g=400$ .

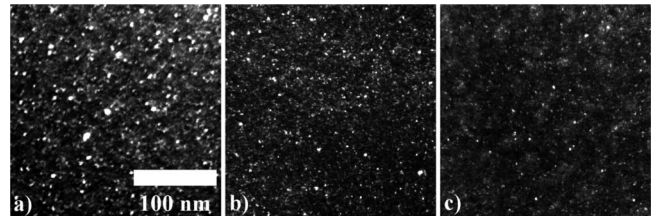


FIG. 3. Set of WBDF-PVTEM images showing the effect of increasing the annealing temperature on a population of EOR defects formed by  $15 \text{ keV } P^+$  and  $1 \times 10^{15} \text{ ions/cm}^2$  implantation. Samples annealed at (a)  $380 \text{ }^\circ\text{C}$  at 30 s, followed by (b) 10 s at  $550 \text{ }^\circ\text{C}$  or (c) 10 s at  $600 \text{ }^\circ\text{C}$ . All images were taken under  $g, 3g$  using  $g=400$ .

size, from 1–2 nm to 4–5 nm in length, while decreasing in density, a trend confirmed by the analysis of WBDF images strictly taken under the same conditions. This observation is similar to what is observed in Si and is consistent with an Ostwald ripening growth mechanism consisting of an interchange of atoms contained in the defects during annealing. This trend was clearly observed on all samples annealed at temperatures lower than  $600 \text{ }^\circ\text{C}$ .

However, the effect of annealing temperature on these populations was different from expected behavior. As an example, Fig. 3 shows the evolution of defects formed by a  $380 \text{ }^\circ\text{C}$  30 s annealing followed by additional annealing for 10 s at  $550 \text{ }^\circ\text{C}$  or  $600 \text{ }^\circ\text{C}$ . While the density of defects decreases during time, the mean size also decreases, from about 4–5 nm to 2 nm, when increasing the annealing temperature. This is contrary to the result expected for a conservative Ostwald ripening mechanism during which the defects grow in size while their density decreases so as to keep the total number of atoms contained within the defects constant. Our observations show that the growth mechanism of these defects is nonconservative, i.e., the population as a whole decreases and this effect increases with the annealing temperature when close to  $600 \text{ }^\circ\text{C}$ .

Finally, it should be noted that the defects seen under WBDF conditions after a typical  $600 \text{ }^\circ\text{C}$  10 s anneal, such as those shown on Fig. 3(c), cannot be detected by high-resolution TEM on cross-sectional samples owing to their very small sizes and low density. We have not succeeded in formally identifying these defects and determining interstitial or vacancy character. With the Ge–Ge bonds being weaker than the Si–Si bonds, the amplitude of the deformation field surrounding a defect in Ge is much smaller than in Si, and more delocalized. Thus, image contrast under WBDF conditions is weaker and more extended than in Si which renders identification through classical contrast rules unreliable. Furthermore, the fault vectors being unknown, the actual defect size distributions and densities cannot be accurately determined. For these reasons, we compared defect populations on images taken under identical imaging conditions to reveal general trends but we could not provide accurate density measurements.

As the character of these defects could not be directly determined, we measured the strain field of the crystalline network in the region where the defects form. For this, we made use of the recently invented imaging technique of dark-field holography.<sup>24</sup> Briefly, this technique consists in forming

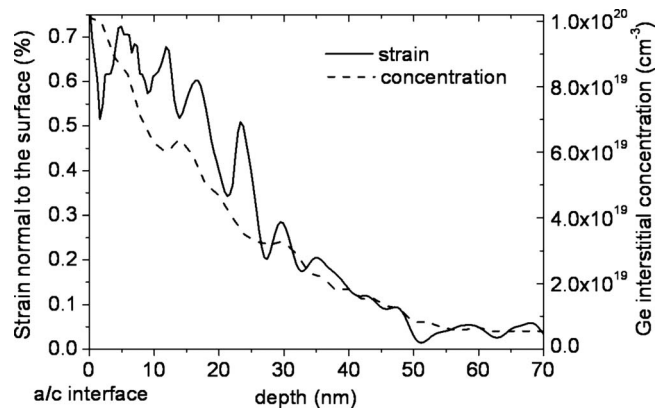


FIG. 4. Plot of  $\epsilon_{zz}$  the lattice strain normal to the wafer surface as measured by electron holography and of the concentration of excess Ge interstitials calculated by MC as a function of distance from the *c/a* interface. The Ge wafer was implanted by Ge<sup>+</sup> at 150 keV with a dose of  $5 \times 10^{14}$  ions/cm<sup>2</sup>.

interference fringes between the diffracted waves emerging from a region of perfectly relaxed Ge crystal and diffracted waves from the (strained) region of interest. The phase shift between these waves can be reconstructed from the interference fringes at every point in the image which can be directly related to the local deformation of the Ge crystalline network with respect to the “perfect” Ge network. Ultimately, this technique can be used to determine the different components of the strain field with nanometer spatial resolution.

We have used this technique to measure the strain field in the region where the defects occur i.e., just below the *c/a* interface. Figure 4 (left axis) shows the variation of the strain field in the direction normal to the wafer surface,  $\epsilon_{zz}$ . Clearly, the lattice is positively strained in this direction and the amplitude of this strain quickly decreases from a maximum of 0.6%–0.7% at the *c/a* interface to below the detection limit (<0.05%) at a depth of 50 nm from this interface. These characteristics are in excellent agreement with those recently reported by Bisognin *et al.*<sup>25</sup> using high resolution x-ray diffraction on similar samples. No deformation was detected in the direction parallel to the wafer surface. These overall characteristics are consistent with the presence of interstitial atoms in the region with the density decreasing moving from the *c/a* interface. It should be noted that any strain possibly induced by the amorphous layer on this crystalline region would be of opposite sign as the density of amorphous Ge is smaller than that of crystalline Ge (though such strains have never been observed experimentally). Finally, as this strain was observed on samples implanted with Ge<sup>+</sup>, the interstitial atoms generating the strain can only be Ge atoms.

To make this point even clearer, we calculated, using Monte Carlo simulations, the concentration of Ge atoms left in excess below the *c/a* interface after a typical 150 keV and  $5 \times 10^{14}$  ions/cm<sup>2</sup> Ge implant.<sup>26</sup> The profile obtained is plotted in Fig. 4 (right axis). It is noticeable that these profiles follow very similar trends and this strongly supports the hypothesis that the observed strain is indeed the result of the presence of Ge interstitials, isolated or within clusters, in the same region.

In conclusion, we have shown that as in Si, the SPER of amorphous layers created by ion implantation in Ge results in the formation of extended EOR defects of interstitial-type. During annealing these defects evolve in size and density following, as in Si, an Ostwald ripening mechanism. The defects are more difficult to observe than in Si, being smaller in size and density, and having significantly weaker image contrast. Nevertheless, imaging was achieved under specific and appropriate imaging conditions. During this Ostwald ripening, the region where the defects occur is supersaturated with free mobile Ge interstitial atoms which can diffuse toward the bulk and the surface of the wafer. Contrary to in Si, defect growth in Ge becomes non conservative when the annealing temperature is increased close to 600 °C. This suggests that the recombination/annihilation of Ge interstitial atoms becomes significant at these temperatures. However, it could not be determined whether these recombinations take place at the surface or within the bulk. This will be the subject of future examination.

However, the observation that interstitial defects exist and evolve during annealing similar those used to activate dopants in Ge has serious implications for diffusion modeling. It is very often considered that only vacancy-assisted diffusion occurs for dopants in Ge. This might not be an intrinsic character of dopant diffusion in Ge but the result of the much larger concentrations of vacancies than interstitials always found under equilibrium conditions. There may be other conditions than those reported here for which the concentration of interstitials is much larger than that of vacancies. This transient contribution of an interstitial assisted mechanism should be included in the models developed to simulate dopant diffusion in ion implanted Ge.

- <sup>1</sup>A. Satta *et al.*, *J. Electrochem. Soc.* **153**, G229 (2006).
- <sup>2</sup>S. Koffel *et al.*, *J. Appl. Phys.* **105**, 013528 (2009).
- <sup>3</sup>S. Koffel, A. Claverie, and P. Scheiblin, *ECS Trans.* **16**, 229 (2008).
- <sup>4</sup>A. Claverie *et al.*, *Appl. Phys. A: Mater. Sci. Process.* **76**, 1025 (2003).
- <sup>5</sup>A. Claverie *et al.*, *Nucl. Instrum. Methods Phys. Res. B* **147**, 1 (1999).
- <sup>6</sup>N. E. B. Cowern *et al.*, *Phys. Rev. Lett.* **82**, 4460 (1999).
- <sup>7</sup>D. J. Eaglesham *et al.*, *Appl. Phys. Lett.* **65**, 2305 (1994).
- <sup>8</sup>C. Bonafos, D. Mathiot, and A. Claverie, *J. Appl. Phys.* **83**, 3008 (1998).
- <sup>9</sup>F. Cristiano *et al.*, *J. Appl. Phys.* **87**, 8420 (2000).
- <sup>10</sup>J. Liu *et al.*, *J. Appl. Phys.* **81**, 1656 (1997).
- <sup>11</sup>I. Martin-Bragado *et al.*, *Solid-State Electron.* **52**, 1430 (2008).
- <sup>12</sup>B. Colombeau *et al.*, *Tech. Dig. - Int. Electron Devices Meet.* **1-2**, 116 (2006).
- <sup>13</sup>A. Satta *et al.*, *Appl. Phys. Lett.* **87**, 172109 (2005).
- <sup>14</sup>A. Satta *et al.*, *J. Vac. Sci. Technol. B* **24**, 494 (2006).
- <sup>15</sup>A. Satta *et al.*, *Appl. Phys. Lett.* **88**, 162118 (2006).
- <sup>16</sup>D. P. Hickey *et al.*, *Appl. Phys. Lett.* **90**, 132114 (2007).
- <sup>17</sup>W. Frank, *Crucial Issues in Semiconductors Materials and Processing Technologies* (Kluwer, Dordrecht, 1992), pp. 383–402.
- <sup>18</sup>M. Werner *et al.*, *Phys. Rev. B* **32**, 3930 (1985).
- <sup>19</sup>S. Koffel *et al.*, *Mater. Sci. Eng., B* **154-155**, 60 (2008).
- <sup>20</sup>M. S. Carroll and R. Koudelka, *Semicond. Sci. Technol.* **22**, S164 (2007).
- <sup>21</sup>C. O. Chui *et al.*, *Appl. Phys. Lett.* **83**, 3275 (2003).
- <sup>22</sup>S. Brotzmann and H. Bracht, *J. Appl. Phys.* **103**, 033508 (2008).
- <sup>23</sup>S. Matsumoto and T. Niimi, *J. Electrochem. Soc.* **125**, 1307 (1978).
- <sup>24</sup>M. Hytch *et al.*, *Nature (London)* **453**, 1086 (2008).
- <sup>25</sup>G. Bisognin *et al.*, *Mater. Sci. Eng., B* **154-155**, 64 (2008).
- <sup>26</sup>IPROS (Monte Carlo simulation of ion implantation into real devices) manual (revised 2007), internal document CEMES/CNRS Toulouse.